NJC

ROYAL SOCIETY OF CHEMISTRY

PAPER

View Article Online
View Journal | View Issue

Cite this: *New J. Chem.*, 2025, 49, 15129

The role of $Ti_3C_2T_x$ MXene in hydrogel engineering for structural organization and ROS scavenging in bacterial models†

Michał Jakubczak, *[a] Iga Niewiadomska,[b] Agnieszka Górnik,[b] Dominika Bury,[a] Marcin Odziomek,[c] Dorota Moszczyńska[b] and Agnieszka Maria Jastrzębska[a]

Received 21st March 2025,
Accepted 23rd July 2025

DOI: 10.1039/d5nj01286d

rsc.li/njc

$Ti_3C_2T_x$ MXene-modified hydrogels offer a unique platform for exploring the interplay between nanomaterials, hydrogel structures, and biological interactions. In this study, we synthesized and characterized 2D $Ti_3C_2T_x$ MXene nanoflakes and integrated them into hydrogel matrices to investigate their impact on structural organization, crosslinking, and interactions with bacterial models. The incorporation of MXenes stabilized the architecture of the hydrogel, particularly in alginate-based matrices lacking chitosan, leading to more organized crosslinking and uniform pore distribution. Chitosan facilitated better MXene nanoflakes dispersion but had a limited effect on structural improvements. Contrary to initial expectations, MXenes did not enhance antibacterial properties. Instead, MXenes exhibited ROS scavenging activity, contributing to increased bacterial viability in both *E. coli* and *S. aureus* models. Notably, alginate/chitosan/elastine hydrogels supported up to 144% viability of *E. coli* after 72 h, highlighting the role of hydrogel structure and redox modulation in microbial interactions. These findings position $Ti_3C_2T_x$ MXene as structural and ROS-modulating components in hydrogel matrices. While these effects were studied in bacterial models, they underscore the material's potential in applications where oxidative stress regulation is relevant, warranting further investigation in mammalian systems.

1. Introduction

Hydrogels are a class of materials composed of water-swollen hydrophobic polymer networks.[1] Depending on the polymer's properties and networking density, these are three-dimensional (3D) structures that can absorb and retain large amounts of water or biological fluids while maintaining their structural integrity.[2,3] Hydrogels can be made from natural (*e.g.*, collagen, lysozyme, gelatin, chitosan, and alginate) or synthetic (*e.g.*, poly(2-hydroxyethyl methacrylate), polyethylene glycol hydrogels, and polyacrylic acid) polymers or a combination of both (hybrid hydrogels) and can be designed to have a wide range of physical, chemical, and biological properties.[3–6]

Hydrogels have a variety of applications in biomedical engineering, such as drug delivery, tissue engineering, wound healing, and biosensing, due to their biocompatibility, tunable properties, and ability to mimic biological tissues.[7,8] For example, Liu *et al.*[9] showed superior adhesion, growth, and proliferation of fibroblast cells by nanocellulose-incorporated hemicellulose hydrogels. Hydrogels have also become a subject of great interest in tissue engineering because they share similarities with the extracellular matrix present in living organisms.[8,10]

Hydrogels can be fabricated into various shapes, such as films, particles, and fibers, which can influence their biodistribution, cellular uptake, and ultimately their delivery efficiency and biocompatibility.[11] Hydrogels modified with functional groups or bioactive molecules, along with mesh size, enhance performance for controlled drug delivery.[11–13] This process can be driven by controlled network degradation, increasing the mesh size for diffusion.[11,14,15] Hydrogels also respond to external stimuli like temperature, pH, and ionic strength by changing their physical properties.[2] According to this concept, Yan *et al.*[16] prepared hydrogels loaded with upconverting nanoparticles. With continuous-wave near-infrared light, they induced the gel–sol transition and released biomacromolecules from the hydrogel network.

A crucial factor influencing hydrogel performance is its internal architecture, which can be tailored using nanostructured additives.[17] Two-dimensional (2D) nanomaterials have emerged as promising candidates for modifying hydrogel networks due to their unique physicochemical properties.[18–20]

[a] *Warsaw University of Technology, Faculty of Mechatronics, św. Andrzeja Boboli 8, 02-525 Warsaw, Poland. E-mail: michal.jakubczak.dokt@pw.edu.pl*
[b] *Warsaw University of Technology, Faculty of Materials Science and Engineering, Wołoska 141, 02-507 Warsaw, Poland*
[c] *Warsaw University of Technology, Faculty of Chemical and Process Engineering, Waryńskiego 1, 00-645 Warsaw, Poland*

† Electronic supplementary information (ESI) available. See DOI: https://doi.org/10.1039/d5nj01286d

Among them, MXenes have attracted significant attention.[21–24] MXenes are a class of 2D transition metal carbides, nitrides, or carbonitrides that were first discovered in 2011.[25] The name MXene is derived from their chemical composition, where 'M' represents a transition metal (*e.g.*, titanium, vanadium, or molybdenum) and 'X' represents carbon and/or nitrogen.[26,27] MXenes are obtained by a top-down approach of selectively etching the 'A' layer (usually aluminum) from layered ternary carbides, nitrides, or carbonitrides known as MAX phases.[25,26]

Due to their tunable surface chemistry, hydrophilicity, and ability to interact with polymers, MXenes have been investigated for improving hydrogel properties beyond their mechanical reinforcement capabilities.[28–30] Their incorporation can influence hydrogel crosslinking, promoting more organized polymeric networks, altering pore morphology, and affecting interactions with biological environments.[31,32] Such modifications can impact the material's biocompatibility, swelling behavior, and stability, making MXene-modified hydrogels an interesting platform for various biomedical applications.

While MXenes have been explored in the context of antimicrobial materials, their broader role in regulating biological interactions remains under investigation.[33–40] One key factor is their ability to modulate reactive oxygen species (ROS) levels, which play a central role in oxidative stress and cellular responses.[34] In mammalian cells, ROS scavenging can be beneficial, reducing oxidative damage and improving cell viability.[41] However, in bacterial systems, where ROS contributes to cellular stress and immune defense mechanisms, the implications of ROS modulation are more complex.[36]

However, before a successful polymer/MXene composite can be developed, several challenges need to be overcome, as mentioned by Carey and Barsoum.[42] Firstly, a polymer matrix (*e.g.*, polyvinyl alcohol) can indeed slow down the oxidation of MXenes; however, it does not completely prevent it.[43] The degree to which MXenes undergo oxidation within a polymeric matrix remains uncertain and is contingent upon the chemistry and/or structure of the polymer.[42] Despite the evident promise associated with modifying a polymeric matrix with MXenes, the constrained availability of MAX phase powders poses a limitation, necessitating the development of novel approaches for manufacturing MXenes.[44]

In this study, we investigated the impact of incorporating $Ti_3C_2T_x$ MXene into hydrogel matrices on their structural organization and biological interactions. Using *Escherichia coli* and *Staphylococcus aureus* as model bacterial strains, we systematically evaluated how MXene modifications influence microbial interactions within a controlled environment. Our findings offer valuable insights into the role of MXenes in shaping hydrogel architecture and modulating biological responses, laying the foundation for future research on nanomaterial-enhanced hydrogels across various biomedical applications.

2. Materials and methods

2.1. Development of the Ti_3AlC_2 MAX phase and $Ti_3C_2T_x$ MXene

The MAX phase used in this study was developed by direct mixing of powders, which were then heated and ground. $Ti_3C_2T_x$ MXene were obtained using an HF/TMAOH approach. The Ti_3AlC_2 MAX phase was soaked in the 48% (v/v) concentrated hydrofluoric acid (HF, Chempur, Piekary Śląskie, Poland) water solution and magnetically stirred at RT for 24 h at 250 rpm. Afterward, the solution obtained went through multiple cycles of washing and centrifugation with deionized (DI) water until a pH of 7 was reached. Delamination was carried out by redispersing collected sediment in a 50% tetramethylammonium hydroxide (TMAOH, Sigma-Aldrich, Saint Louis, MO, USA), which was magnetically stirred at RT for 24 h at 250 rpm. Further, the obtained solution was washed and centrifuged multiple times until the pH reached 7. In the last step, black supernatant containing single 2D $Ti_3C_2T_x$ MXene nanoflakes was collected. Before the use, $Ti_3C_2T_x$ MXene were freeze-dried under vacuum (Alpha 2–4 LD Plus, Martin Christ, Osterode am Harz, Germany) and stored at 5 °C for further use. Details regarding MAX and MXene synthesis are provided in ESI.†

2.2. Characterization of the Ti_3AlC_2 MAX phase and $Ti_3C_2T_x$ MXene

The morphology and structure of the Ti_3AlC_2 MAX phase and $Ti_3C_2T_x$ MXene were evaluated using a Hitachi S-5500 high-resolution scanning electron microscope (HR-SEM, Hitachi, Japan). The samples were redispersed in isopropyl alcohol and then transferred onto copper grids with a thin carbon film. After the evaporation of alcohol samples were studied using an accelerating voltage of 15 kV at various magnifications.

The elemental composition of $Ti_3C_2T_x$ MXene was studied using a Hitachi S-3500N SEM equipped with an energy dispersive spectroscopy (EDS) attachment and an energy-selective backscattered (BSE) detector. Dried samples were transferred onto the surface of sticky copper tape and studied with an accelerating voltage of 15 kV.

The studies of phase transformation of the material during the etching and delamination were carried out with X-ray diffraction (XRD, D8 ADVANCE, Bruker, Billerica, MA, USA). The XRD analysis was conducted utilizing CuKα radiation with a wavelength of $\lambda = 0.154056$ nm, operating at 40 kV voltage and 40 mA current. The angular scan ranged from 5 to 80 degrees with a step of 0.025°.

The chemical composition of both the Ti_3AlC_2 MAX phase and $Ti_3C_2T_x$ MXene was characterized by Fourier transform infrared spectroscopy (FTIR). For this purpose, we used Nicolet iS5 spectrometer (Thermo Scientific, Waltham, MA, USA). The spectrometer was equipped with an attenuated total reflectance (ATR) diamond crystal. The analyses were carried out on freeze-dried samples in the form of powder.

The optical properties of $Ti_3C_2T_x$ MXene were examined with a dual-beam UV-Vis spectrometer Evolution 220 (Thermo Scientific, Waltham, MA, USA). The spectrometer was equipped with an integrating sphere. Measurements were conducted within the wavelength range of 220 to 1100 nm. The measuring parameters were as follows: the integration time of 0.3 s, a resolution of 1 nm, and a scanning rate of 200 nm min^{-1}.

Zeta potential and hydrodynamic diameter measurements were performed using a NANO ZS ZEN3500 analyzer (Malvern

Instruments, Malvern, UK) *via* dynamic light scattering (DLS). All measurements were carried out at 25 °C using a DTS1060 disposable cell. Zeta potential was calculated based on Smoluchowski's model, while particle size was determined using the DLS technique. Each measurement consisted of 10 repetitions, with an acquisition time of 1 s per repetition.

2.3. Development of organic matrix hydrogel composites

Development of the organic matrix hydrogel composites involved preparing stock solutions of 1% (v/v) alginate (ALG), chitosan (CHT), collagen (COL), keratin (KER) and elastin (ELN). Details were provided in the ESI.† The prepared stock solutions were utilized either individually as prepared or mixed in a 1 : 1 ratio to create a composite of ALG and CHT. These prepared solutions were further modified by incorporating 1% (v/v) stock solutions of COL, KER and ELN. To prepare MXene-based composites, 2D nanoflakes of $Ti_3C_2T_x$ in a powder form were added to the developed organic matrix hydrogels, to achieve a final concentration of 1% (v/v). The resulting samples were then freeze-dried under vacuum (Alpha 2–4 LD Plus, Martin Christ, Osterode am Harz, Germany) and subsequently used for further studies.

2.4. Characterization of organic matrix hydrogel composites

The initial observations of developed organic matrix hydrogel composites were carried out with a DMS1000 light microscope (Leica, Wetzlar, Germany). The morphology and structure were studied with a Hitachi S-3500N SEM, using an accelerating voltage from 2.0 to 20 kV. Samples were freeze-dried under vacuum, transferred onto adhesive carbon tape and coated with a 5 nm layer of gold using a BAL-TEC SCD 005 sputter coater (BAL-TEC GmbH, Schalksmühle, Germany).

SEM images were also used to quantitatively assess the porosity of the obtained samples. The image analysis was performed using ImageJ software (National Institutes of Health, NIH, Bethesda, MD, USA). The following parameters were evaluated: average pore size, pore diameter, sphericity factor, maximum and minimum Feret diameter, as well as Feret diameter ratio. Each parameter was determined based on 50 independent measurements. Results were reported as mean value ± standard deviation (SD).

To examine the presence and structural integrity of MXenes within the organic matrix hydrogel composites, we employed a ReactRaman 802L (Mettler Toledo, Greifensee, Switzerland). The measurements were carried out over a range of 150–3400 cm^{-1}, using a 785 nm excitation wavelength and 400 mW excitation power.

The FTIR analysis was employed to identify the organic, polymeric, and inorganic components present in the developed organic matrix hydrogel composites. The analysis was carried out using a Nicolet iS5 FTIR spectrometer. FTIR analysis was performed on powder-like samples, obtained through freeze-drying.

The presence of titanium in the developed organic matrix hydrogel composites was examined using a PI 100 benchtop X-ray fluorescence spectrometer (XRF) from Polon-Izot (Warsaw, Poland). The spectrometer was equipped with a silicon drift detector (SSD) with a resolution of 125–140 eV, a test tube containing a rhodium (Rh) anode, and a multilayer monochromator operating at 50 keV. The investigations were conducted on freeze-dried samples in an air atmosphere, with a measurement time of 300 s per sample and 100 s of measurement normalization. A background measurement was also performed for each sample.

Oscillatory rheological measurements were performed using an Anton Paar MCR 102 rheometer (Anton Paar, Graz, Austria) with a parallel plate geometry (1 mm gap) at 25 °C. A volume of 2.5 mL of each sample was applied onto the lower plate, and the upper plate was lowered to ensure uniform contact. All measurements were conducted at a constant strain amplitude of 0.5% (within the linear viscoelastic region), across an angular frequency range of 10–100 rad s^{-1}. Lower frequencies (0.1–10 rad s^{-1}) were excluded due to significant sample-to-sample variability and poor reproducibility in this regime. Considering the relatively high stiffness of the studied hydrogels, they do not fall into the category of soft hydrogels typically characterized by low-frequency viscoelastic behaviour. Storage modulus (G') and loss modulus (G'') were recorded to assess the viscoelastic properties of the hydrogels. Additionally, complex viscosity (η^*) was calculated based on eqn (1):

$$\eta^* \text{ (Pa s)} = \frac{\sqrt{(G')^2+(G'')^2}}{\omega} \quad (1)$$

where G' is the storage modulus, G'' represents the loss modulus, and ω is the angular frequency.

2.5. Bioactive property studies

The bioactive characteristics of organic matrix hydrogel composites were evaluated using model bacterial strains obtained from the American Type Culture Collection (ATCC). The study involved the use of Gram-negative *Escherichia coli* (*E. coli*, ATCC 10799), and Gram-positive *Staphylococcus aureus* (*S. aureus*, ATCC BAA-231) bacteria strains. Initially, bacteria were grown on tryptic soy agar (TSA, Merck, Darmstadt, Germany) at 37 ± 2 °C for 24 h. Subsequently, bacteria were collected and suspended in sterile phosphate-buffered saline (PBS, Merck, Darmstadt, Germany) to achieve a final concentration of 2 on the McFarland standard scale.

In the next stage, test systems were prepared. To achieve this, samples of organic matrix hydrogel composites were transferred into the 48-well plates (100 μL per well). Further, the test systems were freeze-dried under vacuum. Such prepared samples were then sterilized using a UV-C lamp (Philips, 2 × 30 W, 2.3 W per m^2). Subsequently, prepared bacterial suspensions were added to the test systems (900 μL per well), mixed, and incubated at 37 ± 2 °C for 3 days. After every 24 h, the optical density at 610 nm (OD_{610}) was measured using the multiplate reader Infinite 200 PRO (Tecan, Männedorf, Switzerland). The final results were presented as bacterial viability (V), calculated from eqn (2):

$$V\ (\%) = \frac{OD_{tx}}{OD_{t0}} \times 100 \quad (2)$$

where OD_{tx} is the OD_{610} measured at a given point in time, and OD_{t0} is the OD_{610} measured at time zero.

To validate the accuracy of the OD_{610} measurements of the cultures, control culturing on solid medium was performed. The studies were conducted after 72 h of incubation using the spread-plating technique. To achieve this, 100 μL was collected from each well, and a serial dilution was prepared. Further, 100 μL of each dilution was transferred onto the surface of plate count agar (PCA, Merck, Darmstadt, Germany) and evenly spread using a sterile spreader. Next, Petri plates were incubated at 37 ± 2 °C for 24 h and after that the grown colonies were counted. Results are expressed as the common logarithm (log_{10}) of colony-forming units (CFU), with SD employed to quantify measurement variability.

2.6. Intracellular ROS assay

The presence of intracellular ROS was assessed using a fluorescent indicator. To assess intracellular ROS levels, the general oxidative stress indicator CM-H_2DCFDA (Thermo Scientific, Waltham, MA, USA) was dissolved in dimethyl sulfoxide (DMSO, 99.99% pure, Chempur, Piekary Śląskie, Poland) to achieve a concentration of 0.5 mM. Subsequently, 230 μL of a 72 h test culture was transferred to a multiwell plate, and a fluorescent indicator was added to achieve a final CM-H_2DCFDA concentration of 2 μM in each well. The prepared samples were then incubated in the dark at 37 ± 2 °C for 60 min, and the fluorescence intensity was measured using a microplate reader with excitation and emission wavelengths of 485 and 520 nm, respectively. The levels of intracellular ROS (N) were calculated from eqn (3):

$$N\ (\%) = \frac{A}{B} \times 100 \quad (3)$$

where A represents the fluorescence intensity of the studied sample, and B is the fluorescence intensity of the reference sample.

3. Results and discussion

3.1. Development and characterization of the Ti_3AlC_2 MAX phase and $Ti_3C_2T_x$ MXene

This study focused on the modification of organic-based matrices with 2D $Ti_3C_2T_x$ MXene nanoflakes to understand its role in hydrogel engineering for structural organization and ROS scavenging in bacterial models. $Ti_3C_2T_x$ MXene was synthesized from their parent MAX phase using conventional HF etching and delamination with a TMAOH water solution. Furthermore, to confirm the efficiency of the synthesis and understand the characteristics of $Ti_3C_2T_x$ MXene, we conducted research dedicated for its characterization. The obtained materials were characterized in terms of morphology, structure, elemental and phase composition, optical properties, and chemical composition. The results are presented in Fig. 1 and Fig. S1, S2 and Table S1 (ESI†).

The Ti_3AlC_2 MAX phase is a part of a family of layered ternary compounds. Its crystal structure is hexagonal and belongs to the space group *P*63/*mmc*. In this structure, layers of close-packed titanium (Ti) and aluminum (Al) atoms alternate with carbon (C) layers. Ti and Al atoms are hexagonally packed in a close-packed arrangement, forming the metal layers, while the carbon atoms occupy the octahedral sites between the metal layers.[25–27,45] Thus, under SEM, we should be able to observe a characteristic structure of this material. Analyzing the SEM images of the parental Ti_3AlC_2 MAX phase showed in Fig. 1a and b indeed we observed an atomically thin layered crystal structure, resulting from the stacking sequence of –X–M–X–A- where 'X' represents a carbon layer and 'M' and 'A' represent metal atom layers.[25–27,45] After HF treatment and further delamination in TBAOH water solution, the compact structure of the MAX phase was disturbed, resulting in developing single nanoflakes of $Ti_3C_2T_x$ MXene, as shown in Fig. 1c and d. The obtained nanoflakes were characterized by a rough surface and uneven, wavy edges. However, no surface transformation was observed which could potentially indicate the presence of oxide.

With EDS analysis (Fig. 1e), we confirmed the high purity of developed $Ti_3C_2T_x$ MXene, as well as efficient removal of Al from the parental MAX phase (Fig. S1, ESI†). Based on EDS data, approximately 90.6% of Al was successfully removed during the etching process. The residual Al signal (0.74 at%) likely results from trace unreacted MAX phase or minor surface residues, which are within the typical range reported for HF-based synthesis protocols.[27,46] Moreover, we observed a low oxygen content, primarily associated with the MAX phase itself,[47] a slight oxidation during synthesis[46] and a surface termination of the MXene with oxygen-containing surface groups.[48] Further, we noticed the presence of fluorine, connected with surface termination during the HF treatment. The obtained results align well with the reported data for this synthesis method.[25,45] The XRD results for the Ti_3AlC_2 MAX phase, before and after HF and TMAOH treatment, are shown in Fig. 1f. The XRD pattern obtained from the Ti_3AlC_2 MAX phase shows a hexagonal structure, as suggested by characteristic peaks located at diffraction angles of 9.78, 19.74, 35.21. 37.21, 40.17, 43.25, 50.16, 58.42, 62.71, 67.88, 72.94, and 75.18°. These peaks align well with the (002), (004), (101), (103), (104), (105), (107), (109), (110), (1011), (1012), and (204) planes, respectively. After the HF treatment, the phase composition was substantially disturbed, with the (002) plane transition to 8.30°. Also, the high peak at 60.67° occurred, which corelates with (110) plane and suggests efficient removal of Al and transformation of MAX phase into a multi-layered (ML) MXene.[25] The delamination of ML $Ti_3C_2T_x$ MXene into a single-layered (SL) structure resulted in a further phase transformation, and a characteristic transition of the (002) plane to 5.19° and an increase of the signal, which stands in agreement with reported data.[45,49]

In the subsequent stage of our study, the FTIR analysis (Fig. 1g) demonstrated a high purity of the pristine Ti_3AlC_2 MAX phase, as we did not detect any surface functionalization. However, the synthesized $Ti_3C_2T_x$ MXene exhibited distinctive vibrational peaks, including a C=C bending vibration at 713 cm^{-1}, a C–H bending vibration at 872 cm^{-1}, a C–F stretching vibration at 1403 cm^{-1}, and O–H stretching vibrations at

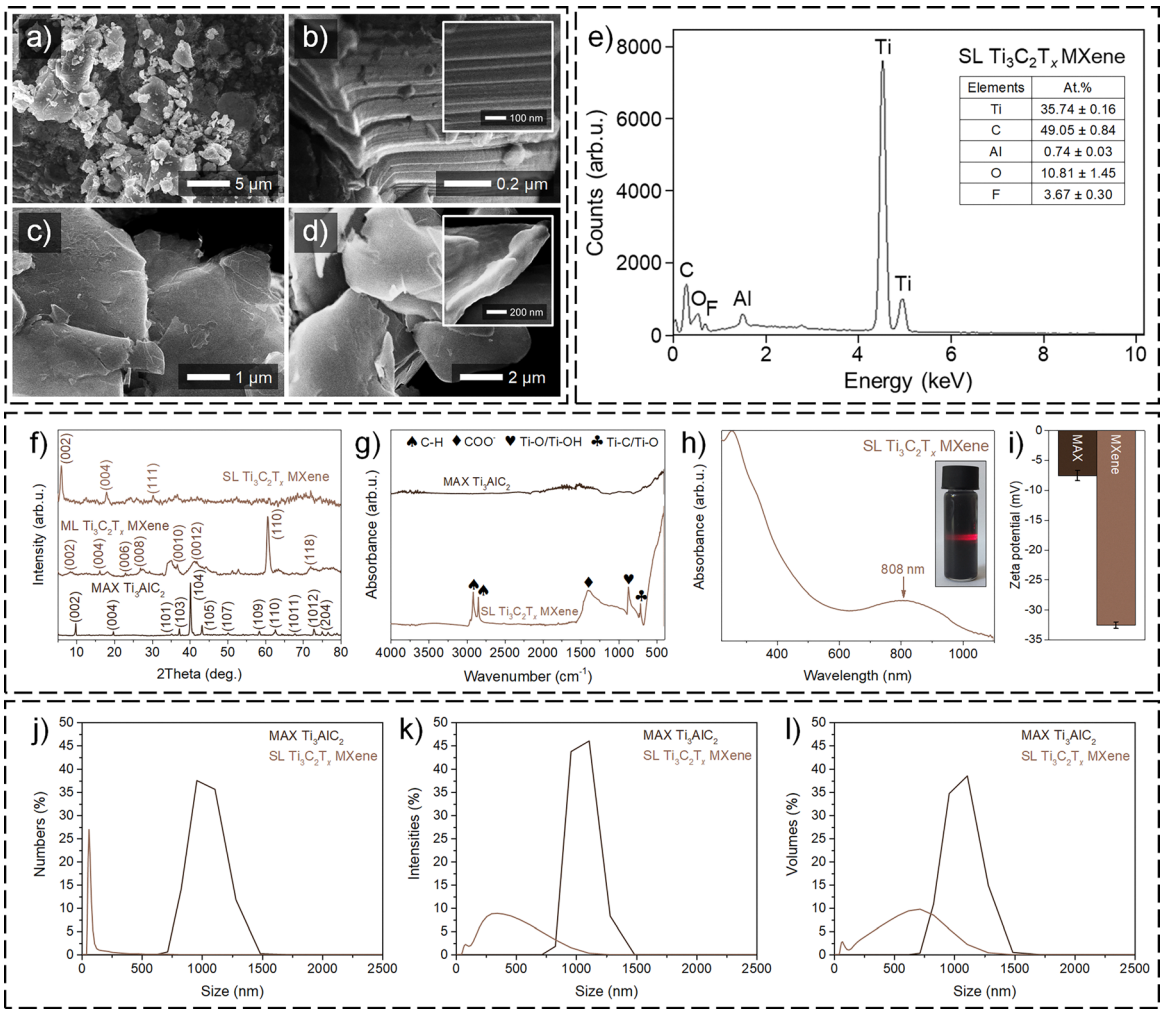

Fig. 1 Characterization of the parental Ti_3AlC_2 MAX phase and the synthesized $Ti_3C_2T_x$ MXene. SEM micrographs of (a) and (b) Ti_3AlC_2 MAX and (c) and (d) $Ti_3C_2T_x$ MXene at different magnifications. (e) Elemental composition analysis of the pristine $Ti_3C_2T_x$ MXene performed *via* SEM-EDS. (f) XRD patterns showing phase transformations during various stages of the $Ti_3C_2T_x$ MXene synthesis. (g) FTIR spectra comparing the chemical compositions of the Ti_3AlC_2 MAX phase and $Ti_3C_2T_x$ MXene. (h) UV-Vis absorption spectrum of $Ti_3C_2T_x$ MXene showing a characteristic plasmonic peak, with inset illustrating the Tyndall effect upon redispersion in water. (i) Zeta potential values for Ti_3AlC_2 MAX and $Ti_3C_2T_x$ MXene water-based dispersions. DLS analysis results for Ti_3AlC_2 MAX and $Ti_3C_2T_x$ MXene presented as (j) numbers, (k) intensities, and (l) volumes distributions.

2848 and 2916 cm^{-1}. The C–F stretching vibration arises from the synthesis procedure, confirming the functionalization with fluorine as previously reported.[42,50] The O–H vibrations are likely associated with confined water molecules.[51,52] Further, we recorded the absorbance spectrum of an aqueous dispersion of $Ti_3C_2T_x$ MXene using UV-Vis spectroscopy (Fig. 1h). The obtained result indicates the presence of a plasmonic peak at 808 nm, which is characteristic of these materials and suggests the effectiveness of the synthesis.[53] $Ti_3C_2T_x$ MXene water-based solution used in the study formed a stable colloidal solution, exhibiting the distinctive Tyndall effect (inset in Fig. 1h).

Zeta potential measurements (Fig. 1i and Table S1, ESI†) revealed a significant change in surface charge following etching and delamination. $Ti_3C_2T_x$ MAX phase water-based dispersion exhibited a zeta potential of −7.53 mV, while $Ti_3C_2T_x$ MXene showed a markedly higher negative value of −32.53 mV, indicating improved colloidal stability. The synthesis also led to an increase in the mobility parameter, indicating that charged MXene particles exhibit higher electrophoretic mobility compared to the parental MAX phase. Additionally, a significant enhancement in conductivity was observed following synthesis.

DLS analysis confirms significant structural changes in the material induced by etching and delamination. The initial particle number distribution (Fig. 1j) shows a disrupted uniformity in Ti_3AlC_2 grains, primarily centered around a hydrodynamic diameter of approximately 1000 nm, forming a Gaussian-like unimodal profile. After delamination, $Ti_3C_2T_x$ MXene exhibit a distinct peak at 62 nm, indicating the formation of smaller, more uniformly dispersed nanoflakes. The intensity distribution, reflecting the relative light scattering from various particle sizes, further supports this transformation. As shown in Fig. 1k, the initial Gaussian-shaped peak for Ti_3AlC_2 shifts to a bimodal distribution post-etching, suggesting increased structural complexity due to multilayer

formation. Volume-based analysis (Fig. 1l) reveals minor agglomeration and a broader size range, evident in a widened peak. These results collectively indicate a clear shift from the original Ti_3AlC_2 morphology, consistent with successful etching and delamination into $Ti_3C_2T_x$ MXene.

Additional studies of the shape parameters for both phases are presented in the ESI† (Fig. S2). These results indicate that the synthesis transformed the material from nearly spherical MAX phase particles into smaller, elongated, nanoflake-like $Ti_3C_2T_x$ MXene nanoflakes, characterized by decreased circularity and Feret widths below 1 μm, consistent with the DLS findings.

3.2. Development and characterization of organic matrix hydrogel composites

After confirming the successful synthesis of $Ti_3C_2T_x$ MXene, we proceeded with our studies. Reported data[54] suggest that the integration of 2D nanomaterials into a hydrogel matrix offers a promising approach for creating advanced materials, improving the characteristics of hydrogels, and overcoming their limitations. Thus, we modified the prepared organic-based hydrogel matrix by incorporating developed $Ti_3C_2T_x$ MXene nanoflakes, with the intention of using it in bacteriological studies. Prior to that, we characterized the composites to confirm the effectiveness of the preparation. Initially, we examined the organic-based matrix hydrogel composites, both before and after modification with $Ti_3C_2T_x$ MXene, using an optical microscope. The results of these observations are presented in the ESI† (check Fig. S3–S6).

ALG-based matrix hydrogel composites exhibited blue-gray, glass-like surfaces with an in-line oriented crosslinking structure (Fig. S3, ESI†). Additionally, we observed the porous structure of these composites. Interestingly, in the case of the ALG/KER composite (Fig. S3c, ESI†), we noticed the influence of the additional polymer on the overall appearance of the composite, resulting in a noticeable darkening. After modification with $Ti_3C_2T_x$ MXene, all composites turned completely dark (Fig. S4, ESI†), suggesting their good dispersion within the matrix. What is even more significant is that an in-line oriented crosslinking structure could only be maintained after modification with additional polymers (COL, KER or ELN). Furthermore, this modification did not affect the porous structure of all composites, which was retained.

On the other hand, ALG/CHT matrix hydrogel composites were characterized by a brown-orange color, resulting from the addition of CHT, and also exhibited glass-like surfaces (Fig. S5, ESI†). However, visually inspecting the orientation of the crosslinking structure and the presence of pores proved to be challenging. Unlike composites without CHT, the addition of such polysaccharides resulted in less pronounced darkening of the final composites modified with $Ti_3C_2T_x$ MXene (Fig. S6, ESI†). We also observed certain spots that were noticeably darker than the rest of the visually inspected samples, likely resulting from the aggregation of MXene nanoflakes.

Further, the SEM imaging technique allowed for a more detailed insight into the morphology and structure of prepared composites. The results are presented in Fig. 2 and Fig. S7, S8 (ESI†). Additional SEM images are shown in Fig. S9–S12 (for details) (ESI†). SEM visualization reveals a characteristic porous structure in both ALG- and ALG/CHT-based matrix composites, resulting from hydrogel crosslinking (Fig. 2a, c and Fig. S9, S11, ESI†). The pores in all composites (Fig. 2a, c and Fig. S7, S8, photos on the left, ESI†) exhibit a large, irregular shape with thick walls and uneven cross-sections. Interestingly, composites without the addition of CHT (Fig. 2a and Fig. S7, ESI†) appear to have much sharper edges of the porous structure. Yet, upon adding this polymer (Fig. 2c and Fig. S8, ESI†), these edges were smoothed, which may be significant in the context of further biological studies.

The introduced $Ti_3C_2T_x$ MXene nanoflakes (Fig. 2b, d and Fig. S7, S8, photos on the right, ESI,† as well as Fig. S10 and S12, ESI†) formed agglomerates ranging from 1 to 5 μm in size. These agglomerates were evenly distributed, covering the surface of the porous structure in the developed composites. The addition of $Ti_3C_2T_x$ MXene nanoflakes also influenced the characteristics of the composites' porous structure. These nanoflakes contributed to stabilizing the hydrogel structure, resulting in more uniform, spherical pores with smoother edges. We suspect that this is attributed to the entrapment of $Ti_3C_2T_x$ MXene nanoflakes within the hydrogel, serving as a scaffold and leading to a more systematic crosslinking.

The SEM analysis also enabled the assessment of porosity in the developed composites. The average pore size (Fig. 2e) and pore diameter (Fig. 2f) sequence of the ALG-based matrix composites is as follows: ALG/KER (2423.19 μm^2 and 54.80 μm), ALG (3973.79 μm^2 and 69.97 μm), ALG/ELN (5327.01 μm^2 and 81.43 μm), and ALG/COL (6040.43 μm^2 and 86.89 μm). The introduction of CHT led to a reduction in average pore size (Fig. 2i) and pore diameter (Fig. 2j), as expected due to the higher polymer concentrations.[55] In addition, there was a change in the porosity parameters sequence to ALG/CHT/COL (581.98 μm^2 and 26.71 μm), ALG/CHT/KER (1218.30 μm^2 and 39.10 μm), ALG/CHT/ELN (2217.64 μm^2 and 52.72 μm), and ALG/CHT (4719.50 μm^2 and 76.29 μm).

Considering the pore shape, composites without CHT exhibited similar sphericity factor values ranging between 0.05 and 0.12 (Fig. 2g), indicating an overall elongated pore morphology. In contrast, the sphericity factor showed greater variability in composites containing CHT (Fig. 2k), increasing in the sequence: ALG/CHT, ALG/CHT/ELN, ALG/CHT/KER, and ALG/CHT/COL, from 0.05 up to 0.16. The elongated shape of the pores was further confirmed by the maximum and minimum Feret diameter (Fig. S13, ESI†), as well as Feret diameter ratio (Fig. 2h and l), which ranged from 0.5 to 0.6 depending on the composite.

The introduction of $Ti_3C_2T_x$ MXene nanoflakes led to a reduction in both average pore size (Fig. 2e and i) and pore diameter (Fig. 2f and j), primarily due to improved crosslinking, with reductions exceeding 60% in some cases, such as the average pore size in the ALG/ELN composite. Interestingly, pore morphology was either maintained or shifted toward more circular shapes, particularly in ALG/CHT-based composites. This is evidenced by higher sphericity factor (Fig. 2g and k) and Feret diameter ratio values (Fig. 2h and l), indicating a

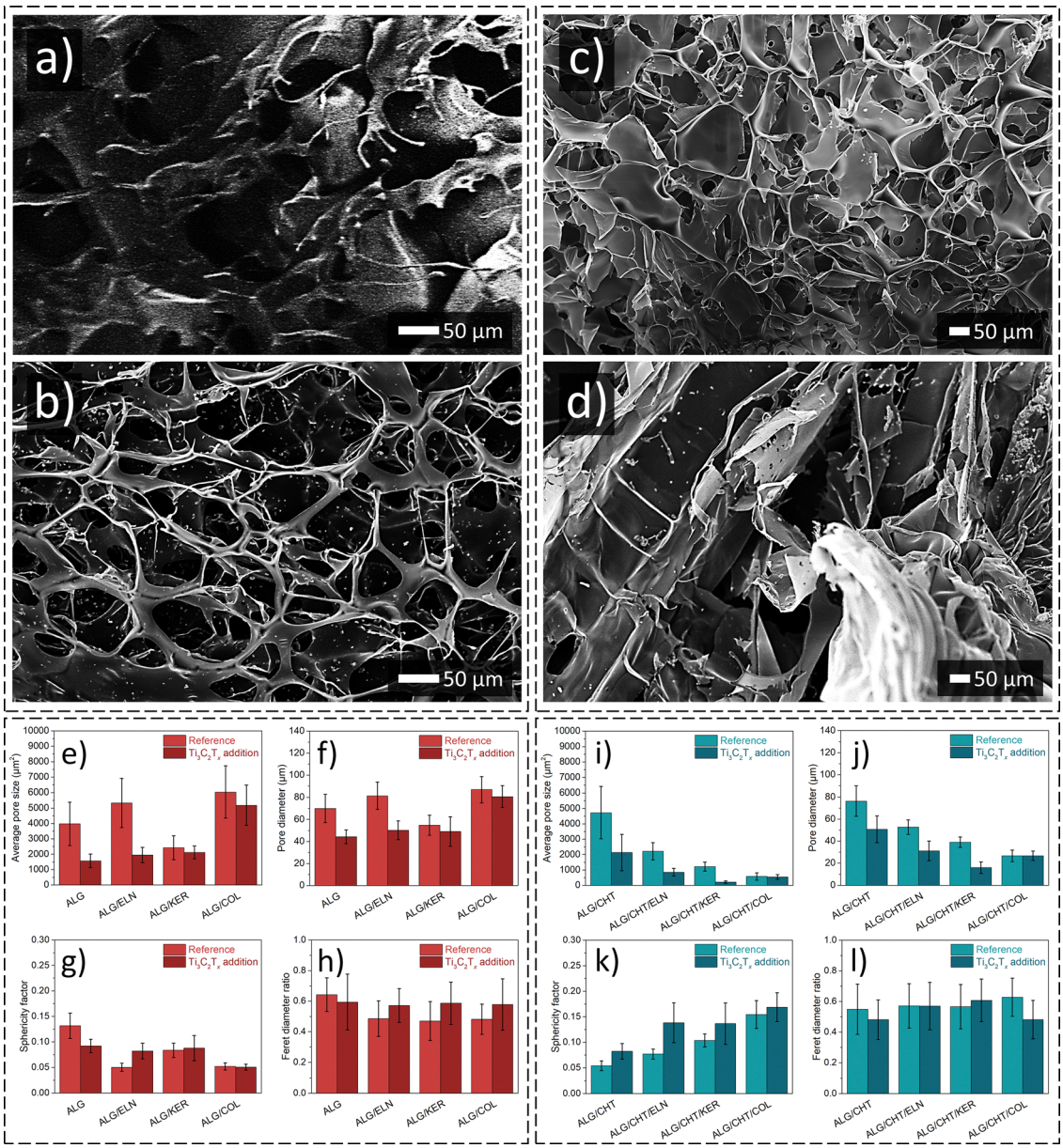

Fig. 2 SEM micrographs of unmodified (a) ALG- and (c) ALG/CHT-based matrix composites, as well as (b) ALG- and (d) ALG/CHT-enriched with $Ti_3C_2T_x$ MXene nanoflakes. Porosity analysis including (e) and (i) average pore size, (f) and (j) pore diameter, (g) and (k) sphericity factor, and (h) and (l) Feret diameter ratio for (e–h) ALG- and (i–l) ALG/CHT-based composites.

transition from elongated to more uniform, spherical pores. These observations support SEM analysis, which showed that the presence of $Ti_3C_2T_x$ MXene nanoflakes contributed to stabilizing the hydrogel structure, resulting in more uniform, rounded pores with smoother edges, providing structural support and facilitating the uniformity of crosslinking. Janeček *et al.*[56] demonstrated that incorporating nanomaterials into hydrogels can enhance crosslinked networks or endow hydrogels with specific biological properties. Such modifications can also improve the mechanical properties and introduce additional functionalities, such as drug delivery potential.[57] Nanomaterials added to the crosslinked network serve as the gel skeleton, and their stiffness contributes to the mechanical properties of the hydrogel.[57,58] Another thing to consider is that conventional crosslinking agents may cause irreversible crosslinking, impacting self-healing capabilities and consequently restricting the potential applications of hydrogels, like in tissue scaffolds and drug delivery. This supports the utilization of nanomaterials, which not only improves the final product but also diminishes the requirement for typical crosslinking agents.[59–61]

This study aimed to develop $Ti_3C_2T_x$ MXene-modified hydrogel composites to understand MXenes role in tunning hydrogels bioactivity using bacterial models. Therefore, it is worth noting that the presence of functional groups can significantly impact the bioactive properties of materials towards bacteria.

For example, functional groups such as amino groups, phenolic groups, or compounds containing silver ions can confer antibacterial properties to materials, inhibiting the growth and development of bacteria.[62] Therefore, the subsequent part of our work focused on analyzing the surface chemistry of the developed materials using Raman and FTIR spectroscopy to evaluate the efficient incorporation of the $Ti_3C_2T_x$ MXene into the hydrogel matrices and its interaction with organic components. While XPS is widely regarded as the gold standard for surface-specific chemical analysis, the combined use of Raman and FTIR spectroscopy provides a complementary and, in some aspects, superior approach for characterizing complex hydrogel systems. These vibrational techniques allow for the detection of both surface and bulk chemical environments, capturing interactions that extend beyond the shallow probing depth of XPS.[63,64] This is particularly advantageous in hydrated, porous matrices like hydrogels, where surface-bulk boundaries are diffuse and chemically interconnected.[63,65] The results obtained are presented in Fig. 3a–d.

In both Raman and FTIR spectra, the organic matrix hydrogels exhibited characteristic vibrational modes typical of ALG- and CHT-based biopolymers, confirming the expected molecular structure of the organic matrix. Details can be found in the ESI† (Fig. S14–S15). These reference profiles provide a reliable baseline for assessing the chemical changes induced by MXenes incorporation and biomacromolecule functionalization.

In Raman spectra, composites enriched with $Ti_3C_2T_x$ MXene (Fig. 3a and b) displayed a series of characteristic vibrational modes at 212, 375, 417, 449, 509, 577, 622, 727, and 749 cm^{-1}.[66,67] The most prominent bands of 417, 449, 577 and 749 cm^{-1} can be assigned to Ti–O surface terminations, out-of-plane Ti–C–O and Ti–O deformations, as well as Ti–C in-plane vibrations, respectively.[67] Upon MXenes incorporation, the spectral profiles of both ALG- and ALG/CHT-based composites became dominated by these $Ti_3C_2T_x$ MXene-specific peaks, closely mirroring those of the pristine nanoflakes and confirming its successful integration into the hydrogel networks. Notably, no additional peaks indicative of biopolymer degradation or unfavorable structural changes were detected. These results support the structural integrity and chemical activity of MXenes within a composite system.

FTIR spectra complemented the Raman data by highlighting changes in the organic component. In ALG-based hydrogels (Fig. 3c), strong bands near 1025, as well as 1405 and 1601 cm^{-1}, correspond to C–O–C stretching vibrations of the pyranose ring and symmetric COO^- stretching of alginate carboxylate groups. Upon $Ti_3C_2T_x$ MXene modification, additional bands emerged, notably at 619 (Ti–C or Ti–O), 811 (Ti–O or Ti–OH), 896 (C–O–C), 946, 1092, 1127 (C–O–C or C–OH), as well as broad O–H and N–H stretching around 3292 cm^{-1}.[68] These suggest hydrogen bonding or electrostatic interactions between MXene surface groups (–OH, –F, –O) and the polysaccharide chains.[69]

In ALG/CHT-based composites (Fig. 3d), MXenes introduction led to bands at 1029, 1069 cm^{-1} (C–O and C–N stretching), 1523 cm^{-1} (amide II), and a complex pattern between 1964–2162 cm^{-1}, potentially related to overtone and combination modes or weakly IR-active Ti-bound surface functionalities.[68–70] Overall, the FTIR and Raman analyses confirm the successful incorporation of $Ti_3C_2T_x$ MXene nanoflakes into both hydrogel types and reveal interfacial chemical interactions that may influence the mechanical and biofunctional properties of the composites.

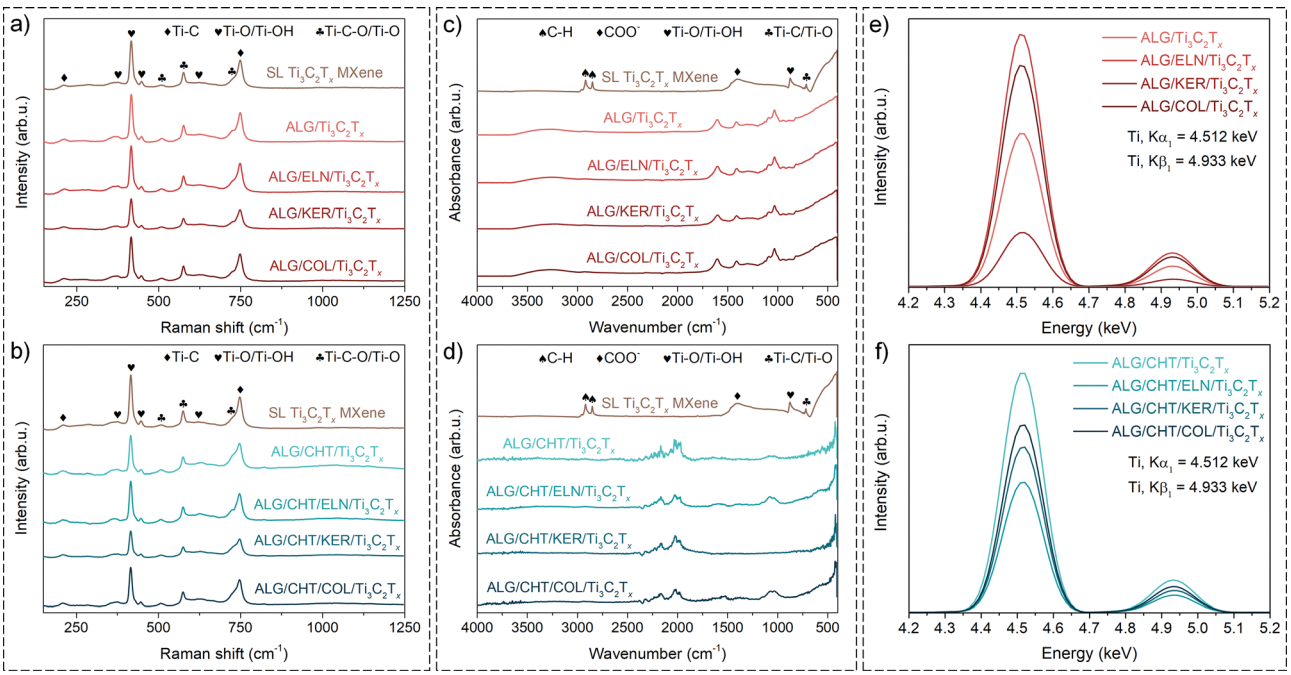

Fig. 3 The analysis of the efficiency of $Ti_3C_2T_x$ MXene incorporation into hydrogel matrices, considering (a), (c) and (e) ALG- and (b), (d) and (f) ALG/CHT-based matrix composites. Samples were analyzed using (a) and (b) Raman, (c) and (d) FTIR, and (e) and (f) XRF spectroscopy.

Although the SEM analysis enabled us to assess the morphology and structure of the organic-based matrix hydrogel composites, both before and after modification with $Ti_3C_2T_x$ MXene, it did not provide information about the internal distribution of the nanoflakes. Yet, it is worth noting, that with SEM, we observed an even distribution of the MXene nanoflakes and their beneficial impact on the crosslinked network, acting as the gel skeleton. Therefore, in the subsequent part of our research, we aimed to verify the presence of $Ti_3C_2T_x$ MXene nanoflakes in the organic-based matrix hydrogel composites and assess the extent to which the nanoflakes were concealed within the matrix. To achieve this, we utilized the XRF technique, which enabled us to detect titanium signals indicative of MXene incorporation. The corresponding results are presented in Fig. 3e and f, respectively.

The performed XRF measurements enabled us to identify differences in signal intensities, indicating varying degrees of incorporation of $Ti_3C_2T_x$ MXene nanoflakes within the structure of the organic-based matrix hydrogel composites and varying quantities of them on their surface. A higher content of $Ti_3C_2T_x$ MXene on the surface results in a higher intensity of the Ti signal, whereas concealing the nanoflakes deep within the structure of hydrogels lowers the Ti signal intensity, which is associated with the attenuation effect or electrons scattering due to the created organic shell.[71,72] Following this line of thought, in the case of ALG-based matrix hydrogel composites, ALG/KER showed the highest level of concealment, while for ALG/ELN, there was the least attenuation due to the presence of the organic matrix (Fig. 3e). Adding CHT to the ALG-based hydrogel matrix allowed for a more even distribution of $Ti_3C_2T_x$ MXene nanoflakes within the developed composites, as the Ti signal intensity is much more consistent within them (Fig. 3f). We observed the lowest level of concealment for ALG/CHT composites, without additional polymers. However, the ALG/CHT/ELN composite was characterized by the lowest intensity of the Ti signal, suggesting the highest level of concealment.

The viscoelastic properties of the hydrogel formulations were evaluated by oscillatory rheometry, recording both storage modulus (G') and loss modulus (G'') across a range of angular frequencies (10–100 rad s^{-1}) to assess their mechanical stability and behavior under dynamic conditions, which is crucial for their potential biomedical applications. The rheological response was strongly dependent on the formulation composition, revealing distinct mechanical characteristics (Fig. 4a–d). Formulations such as ALG alone or combined with a single structural protein (CHT, COL, and KER) or their binary combinations (*e.g.*, ALG/CHT/KER or ALG/ELN) exhibited nearly equal values of G' and G'' throughout the frequency range, suggesting a viscoelastic balance indicative of weak or loosely crosslinked gels. In contrast, the addition of $Ti_3C_2T_x$ MXene to multicomponent systems, particularly those containing CHT, shifted the mechanical profile toward an elastic-dominated behavior, with G' significantly exceeding G''. This was especially pronounced in formulations such as ALG/CHT/$Ti_3C_2T_x$, ALG/CHT/KER/$Ti_3C_2T_x$, and ALG/CHT/ELN/$Ti_3C_2T_x$, where the presence of MXenes appeared to act as an effective physical crosslinker, enhancing both network stiffness and energy dissipation capacity. The strongest elastic response was observed for ALG/CHT/COL/$Ti_3C_2T_x$ and ALG/CHT/KER/$Ti_3C_2T_x$, which reached G' values exceeding 200 Pa at high frequencies, reflecting robust internal structuring and resistance to deformation.

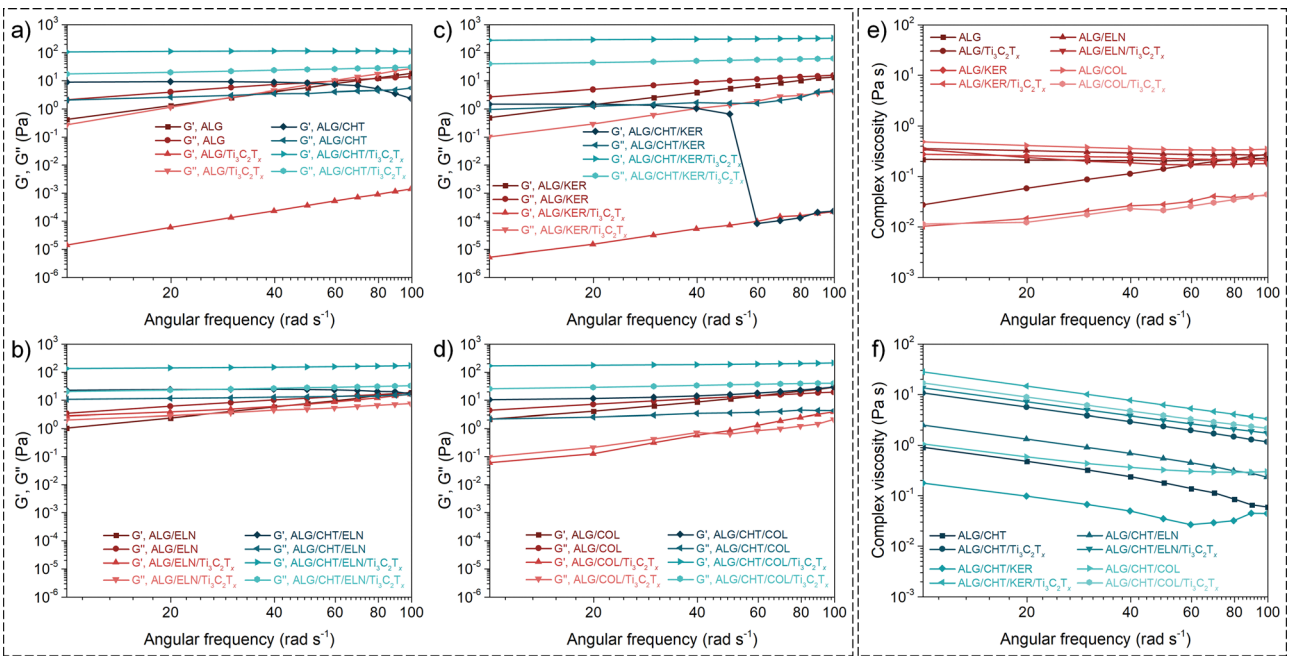

Fig. 4 Oscillatory rheological measurements considering storage modulus (G') and loss modulus (G'') for (a) ALG- and ALG/CHT-, (b) ALG/ELN- and ALG/CHT/ELN-, (c) ALG/KER- and ALG/CHT/KER-, and (d) ALG/COL- and ALG/CHT/COL-based matrix composites, completed with complex viscosity measurements performed for (e) ALG- and (f) ALG/CHT-based matrix composites.

Conversely, some MXene-containing systems, such as ALG/$Ti_3C_2T_x$, ALG/COL/$Ti_3C_2T_x$, and ALG/KER/$Ti_3C_2T_x$, showed a predominance of viscous behavior ($G'' > G'$), indicating that in the absence of chitosan or other structural biopolymers, the incorporation of $Ti_3C_2T_x$ alone was insufficient to induce elastic gel formation. This highlights the importance of matrix composition and the need for synergistic interactions between components to achieve desirable mechanical performance.

The complex viscosity exhibited distinct trends depending on the hydrogel composition. In samples based on ALG alone or its binary composites without MXenes (Fig. 4e), complex viscosity decreased with increasing frequency, indicating shear-thinning behavior characteristic of physically crosslinked polymer systems with limited structural reinforcement. In contrast, ALG/$Ti_3C_2T_x$, ALG/COL/$Ti_3C_2T_x$, and ALG/KER/$Ti_3C_2T_x$ formulations showed an increase in complex viscosity by approximately an order of magnitude relative to their initial values, suggesting a frequency-dependent thickening effect and a more pronounced viscous contribution, likely due to insufficient matrix stabilization in the absence of additional biopolymers. Meanwhile, all formulations containing CHT (Fig. 4f) demonstrated a decreasing complex viscosity profile across the frequency range, confirming strong shear-thinning behavior and effective network formation, likely enhanced by electrostatic interactions and hydrogen bonding between components.

3.3. Bioactive property studies

The information obtained so far, such as the smoothing of the porous structure edges and the presence of neutral functional groups, suggests that the developed materials are more likely to be biostatic rather than antibacterial. So far, the only reason they could attribute antibacterial properties is the likely presence of titanium oxide (TiO_2) forming on the MXene surface due to the so-called aging.[35,39] Numerous studies indicate that, besides the sharp edges, the presence of TiO_2 exhibiting biocidal characteristics on the surface of $Ti_3C_2T_x$ MXene

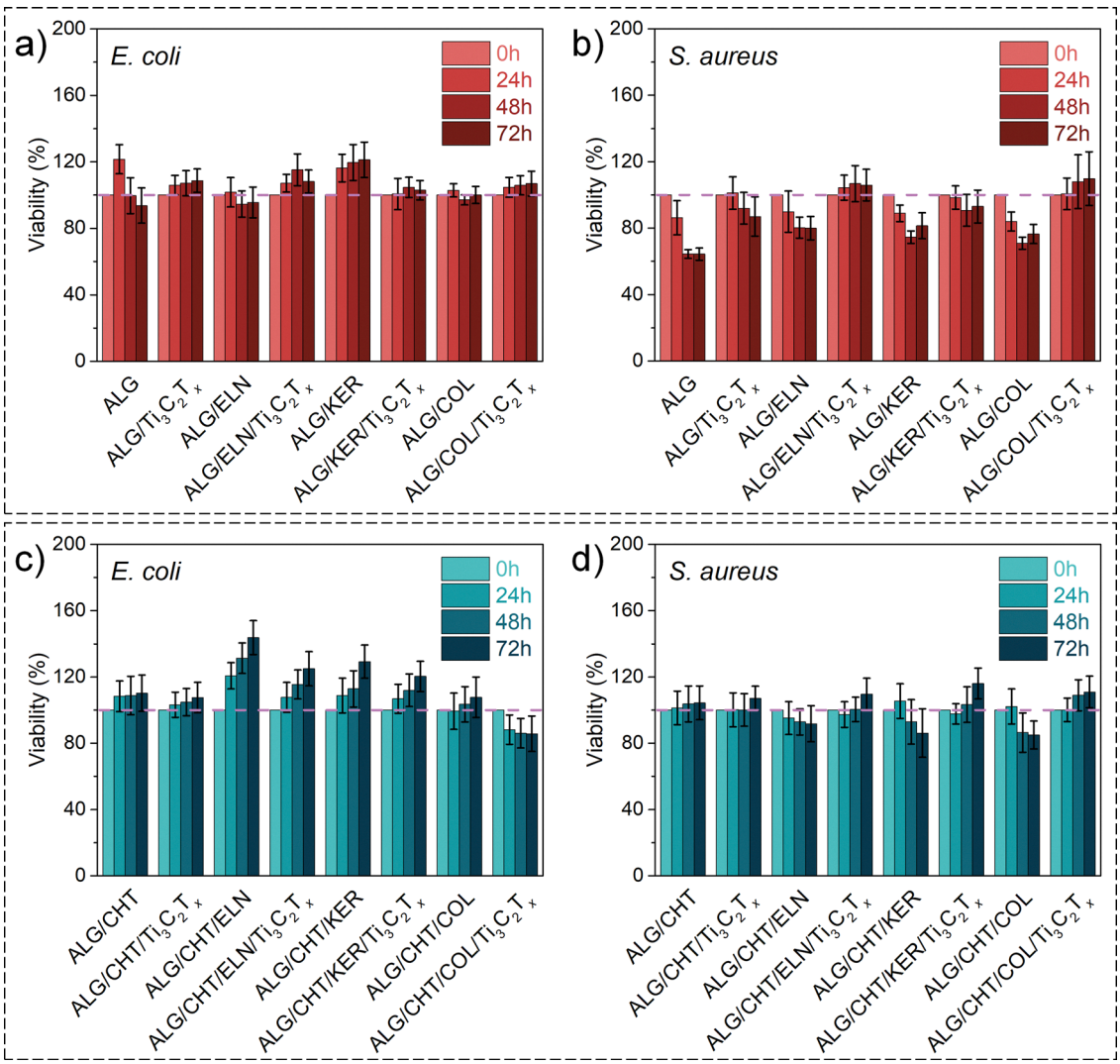

Fig. 5 Bioactive properties of (a) ALG- and (b) ALG/CHT-based organic matrix composites assessed by viability assays against *E. coli*, and (c) ALG- and (d) ALG/CHT-based composites evaluated against *S. aureus*.

nanoflakes is the primary factor contributing to the antibacterial properties of this material. Despite its small quantity and expected biostatic effect, we proceeded with bacterial research. To achieve this, we used models of potentially pathogenic bacteria, namely *E. coli* and *S. aureus*. The results of this analysis are illustrated in Fig. 5.

In the case of ALG-based matrix hydrogel composites and *E. coli* bacteria (Fig. 5a), we observed that the organic matrices were predominantly biostatic. However, for pure ALG and ALG/ELN composite, we noted a slight reduction in bacterial viability (approximately 4–6% based on measurements taken after 72 h). Modification of ALG-based matrices with $Ti_3C_2T_x$ MXene allowed for the maintenance of *E. coli* bacterial viability at 100% and even enabled a slight, consistent multiplication of the mentioned bacteria. For instance, in measurements taken after 72 h for the ALG/COL/$Ti_3C_2T_x$ composite, we observed that the viability of *E. coli* increased to about 106%. In contrast, for *S. aureus* bacteria (Fig. 5b), all ALG-based matrices exhibited a slight antibacterial effect, reducing bacterial viability by 20–36% (depending on the studied material composition). Modification with $Ti_3C_2T_x$ MXene allowed for the adjustment of their biostatic properties. Even in the case of ALG/ELN/$Ti_3C_2T_x$ and ALG/COL/$Ti_3C_2T_x$ composites, we observed that these composites were able to maintain *S. aureus* viability above 100% (approximately 6–10% based on measurements taken after 72 h).

Alginate-based organic matrices appeared slightly different bioactive properties after CHT was introduced (Fig. 5c). All pure ALG/CHT-based organic matrices facilitated the multiplication of *E. coli* bacteria, resulting in final viabilities reaching as high as 144%, as observed in the case of the ALG/CHT/ELN composite in measurements taken after 72 h. The modification with $Ti_3C_2T_x$ MXene decreased the biocompatibility of the developed ALG/CHT-based organic matrices. In this manner, the viability of *E. coli* was reduced even by up to 22% (in comparison to unmodified matrices), as observed in the case of the ALG/CHT/COL composite. Furthermore, this composite exhibited antibacterial properties, resulting in a final *E. coli* viability of 86%. In the studies conducted with *S. aureus* bacteria on the ALG/CHT-based organic matrices (Fig. 5d), we observed a reversal of the bacterial interaction trend. Initially, ALG/CHT-based organic matrices (excluding pure ALG/CHT) exhibited mild antibacterial properties, leading to a reduction in *S. aureus* viability by 10–15%. The incorporation of $Ti_3C_2T_x$ MXene into ALG/CHT-based organic matrices proved to be a game-changer, significantly enhancing *S. aureus* viability by 18–30%, as evidenced by measurements taken after 72 h.

Improving the biocompatibility of hydrogels is fundamental to advancing their use in biomedical applications, ensuring safety, efficacy, and successful integration with biological systems for improved patient care and outcomes.[73,74] Shao *et al.*[75] reported a hydrogel modification using black phosphorus (BP), targeting the removal of residual cancerous tissue. They demonstrated that the gelation of the hydrogel structure and properties remained unaffected by the incorporation of BP, and it exhibited *in vitro* biocompatibility with human mesenchymal stem cells (hMSCs), L929, and HeLa cells. Xiang *et al.*[76] developed cellulose hydrogels modified with $T_3C_2T_x$ MXene. They stated that this hydrogel displayed excellent biocompatibility while also demonstrating a notable efficiency in converting light to heat for tumor ablation, both *in vitro* and *in vivo*. Ningrum *et al.*[77] modified polyvinyl alcohol with graphene oxide for use in wound dressing applications. They noticed improved biocompatibility with studies on 3T3-L1 mouse fibroblast cells. Yet, to allow their antibacterial action, the *Moringa oleifera* leaf extract was needed.

Our studies on bacterial viability demonstrated enhanced biocompatibility of the developed organic-matrix hydrogel composites. However, we acknowledge that the OD_{610} method, despite its obvious advantages, only estimates bacterial growth and does not offer specific information about growth characteristics. With this in mind, we carried out subsequent work to validate the obtained results using the culturing method. For that, we utilized PCA and Petri plates for the samples incubated in the presence of organic-matrix hydrogel composites for 72 h. The results are presented in Fig. S16 (ESI†).

Generally, microbiological analysis involving culturing on solid medium confirmed the results obtained from the OD_{610} tests. In the case of *E. coli* bacteria (Fig. S16a and c, ESI†), the modification of organic-based hydrogel matrices led to a higher number of bacterial colonies, and therefore their enhanced survival rate. The most significant differences due to the presence of $Ti_3C_2T_x$ MXene nanoflakes were observed in ALG without any additional polymers and the ALG/ELN composite. In the case of a pure ALG matrix, the presence of $Ti_3C_2T_x$ MXene improved its antibacterial properties, manifested by a significant reduction in the number of CFU. However, for the ALG/ELN composite, the situation was reversed; the addition of $Ti_3C_2T_x$ MXene resulted in an increase in the number of *E. coli* colonies grown by an order of magnitude, thereby improving biocompatibility. Also, in the case of *S. aureus* bacteria, additional analysis through culturing confirmed the results obtained from the OD_{610} measurements (Fig. S16b and d, ESI†). The results show that modification with $Ti_3C_2T_x$ did not impact the number of CFU or could even improve the survival rate of *S. aureus* in the presence of the developed composites. Only in the case of the ALG/CHT/COL composite, we observe a lower number of CFU by order of magnitude, indicating that the presence of $Ti_3C_2T_x$ MXene could potentially slightly disrupt the viability of *S. aureus*.

3.4. Intracellular ROS assay

To elucidate the stabilizing (in terms of biocompatibility) properties of $Ti_3C_2T_x$ MXene when incorporated into the organic-matrix hydrogel composites, we conducted intracellular ROS studies. In the context of the analysis, ROS levels were calculated in accordance with unmodified organic-based hydrogel matrices. It is clear that if incorporating $Ti_3C_2T_x$ results in increased biocompatibility, it should also reduce intracellular ROS, increased levels of which can be easily correlated with bacteria immobilization. Fig. 6 represents the results of conducted studies.

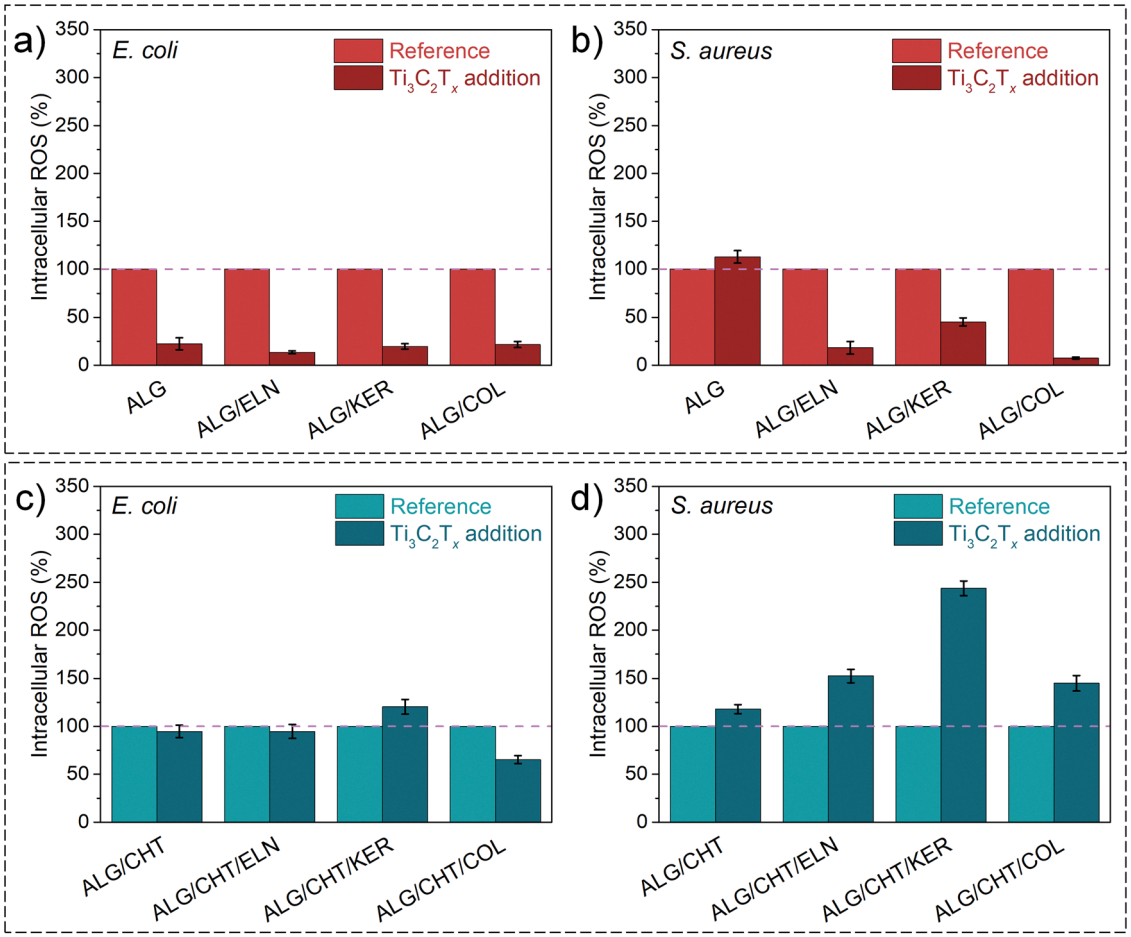

Fig. 6 Level of intercellular ROS detected for the (a) and (c) *E. coli* and (b) and (d) *S. aureus* bacteria incubated in the presence of (a) and (b) ALG- and (c) and (d) ALG/CHT-based organic matrix hydrogel composites and measured after 72 h of incubation.

In that context, we investigated the modulation of intracellular ROS in ALG-based hydrogel matrices due to the presence of $Ti_3C_2T_x$ MXene (Fig. 6a and b). In the case of *E. coli* bacteria, we observed that the modification led to a significant reduction in the levels of intracellular ROS for all of the prepared composites, ranging from 78% in the case of ALG/$Ti_3C_2T_x$ and ALG/COL/$Ti_3C_2T_x$, up to 87% for ALG/ELN/$Ti_3C_2T_x$. Such properties were also maintained in the case of *S. aureus* bacteria, as the modification of the ALG/COL composite with $Ti_3C_2T_x$ MXene allowed for a reduction of the intracellular ROS level by 92%. Only in the case of unmodified ALG, we observed a slight (by almost 13%) increase in intracellular ROS level. Interestingly, in the case of ALG/CHT-based hydrogel matrices and *E. coli* bacteria (Fig. 6c), the addition of $Ti_3C_2T_x$ MXene did not allow for such a robust modulation of intracellular ROS levels. Measurements performed for the ALG/CHT/COL/$Ti_3C_2T_x$ composite showed a reduction of 35%. For the rest of the composites, such reduction did not exceed 5%, and in the case of the ALG/CHT/KER/$Ti_3C_2T_x$ composite, the intracellular ROS level even increased by 20%. What is more, results from the studies performed on *S. aureus* (Fig. 6d) suggest that modification with $Ti_3C_2T_x$ MXene did not allow for the reduction of intracellular ROS levels at all. Similar to the studies performed on *E. coli*, for the ALG/CHT/KER/$Ti_3C_2T_x$ composite, the intracellular ROS level increased (by approximately 2.5 times), suggesting the antibacterial potential of this hydrogel composition.

These differences in ROS modulation can be attributed to the electrostatic interactions between the negatively charged $Ti_3C_2T_x$ MXene nanoflakes and the positively charged chitosan molecules.[78] The strong attraction between these components likely leads to changes in surface charge distribution and partial masking of MXenes reactive sites, which diminishes their intrinsic ROS scavenging ability.[79,80] As a result, composites containing chitosan exhibit sustained or even elevated intracellular ROS levels, correlating with increased antibacterial activity.

Furthermore, the high surface area and reactive oxidative vacancies of $Ti_3C_2T_x$ MXene enable effective adsorption and neutralization of reactive oxygen species such as hydroxyl radicals ($^{\bullet}OH$) and superoxide anions (O_2^-).[81–84] This explains the superior ROS scavenging observed in ALG-based composites without CHT, where MXenes surface sites remain more accessible. Conversely, the incorporation of positively charged biopolymers, such as chitosan, alters the redox balance by electrostatically modulating MXenes surface charge and reactivity, reducing its antioxidant properties.

In general, hydrogels are not known to inherently generate intercellular ROS.[13] However, it is important to note that the interaction of hydrogels with biological systems can trigger responses at the cellular level. For example, Fu *et al.*[85] reported, that hydrogels intended for bone tissue regeneration may induce inflammatory responses. Yet, Kim and Kim[86] noticed the necessity of developing a composite hydrogel with significant ROS consumption to promote wound healing. While ROS plays a crucial role in cellular processes, an excess of them could potentially trigger numerous inflammatory diseases due to the oxidation of proteins, DNA, and membrane lipids.[87] Strategies for imparting antioxidant characteristics to hydrogels involve incorporating catalytic nanomaterials that scavenge ROS, altering hydrogel polymer chains with organic moieties that adsorb ROS, and integrating ROS-sensitive linkers within the polymer structure.[86,88] Simultaneously, Liu *et al.*[84] reported that $Ti_3C_2T_x$ MXene acts as a free-radical scavenger. More importantly, they demonstrated that the presence of $Ti_3C_2T_x$ allowed for protecting the alpha mouse liver 12 (AML12) cells from oxidative damage. Free-radical scavenging properties of $Ti_3C_2T_x$ MXene were also confirmed by different groups.[81–83]

While intracellular ROS modulation explains a significant portion of the observed bioactive behavior, it does not fully account for all observed effects. As highlighted in Tables S2 and S3 (ESI†), some hydrogel composites exhibit strong antibacterial activity even in the absence of notable ROS level reduction. For instance, the addition of ELN or KER to ALG/CHT matrices resulted in a positive impact on the growth of *E. coli*, despite minimal or even slightly elevated levels of intracellular ROS levels. Notably, the incorporation of COL into ALG/CHT matrices led to divergent effects: a decrease in bacterial viability in some cases, yet no consistent ROS modulation. This suggests that these additives may influence bacterial cell adhesion, membrane permeability, or local microenvironmental conditions through mechanisms independent of oxidative stress.[89] It also underscores the multifactorial nature of antibacterial performance in composite hydrogels.[90] The interplay between polymeric components, surface charge distributions, and protein-based additives can result in synergistic or antagonistic effects that are not solely governed by ROS scavenging.[91]

4. Conclusion

The development of hydrogels modified with 2D nanomaterials has been widely explored for biomedical applications, particularly in wound healing and tissue engineering, due to their ability to enhance mechanical properties, provide biocompatibility, and allow for functionalization. In this study, we successfully synthesized $Ti_3C_2T_x$ MXene from Ti_3AlC_2 MAX phase using HF etching and subsequent delamination in a TMAOH water solution. The resulting material was thoroughly characterized, confirming its layered morphology, phase transformation, and stable composition.

Incorporating $Ti_3C_2T_x$ MXene into hydrogel matrices resulted in notable structural modifications. SEM imaging demonstrated that the typically irregular, sharp-edged porous architecture of unmodified hydrogels transformed into a more uniform network with smoother pore edges upon MXenes introduction. This suggests that nanomaterials influenced the hydrogel's crosslinking process, facilitating a more organized network formation.

The incorporation of MXenes into ALG-based hydrogels significantly reduced pore size and diameter, while promoting a transition from elongated to more circular pore morphologies, particularly in CHT-containing composites. These structural changes, confirmed by sphericity and Feret diameter analyses, suggest enhanced crosslinking and matrix stabilization, contributing to a more uniform and robust hydrogel architecture.

Chemical and structural analyses confirmed the successful incorporation of MXenes into the hydrogel matrices. Raman and FTIR spectra revealed distinct $Ti_3C_2T_x$ MXene-specific vibrational modes, particularly Ti–O, Ti–C–O, and Ti–C bands, without signs of biopolymer degradation, indicating effective embedding without compromising the organic matrix. Additionally, new FTIR bands and shifts suggested hydrogen bonding and electrostatic interactions between nanoflakes surface groups and the hydrogel components, highlighting interfacial chemical integration that may underlie the enhanced mechanical performance of the composites. XRF measurements verified its presence in all modified formulations, though with varying degrees of distribution within the polymeric network.

The rheological analysis demonstrated that the viscoelastic properties of the hydrogels were highly dependent on formulation composition, with chitosan and $Ti_3C_2T_x$ MXene playing key roles in enhancing network elasticity and structural integrity. Notably, the synergistic combination of CHT and MXene nanoflakes resulted in robust, shear-thinning hydrogels with elastic-dominated behavior, emphasizing the importance of multi-component interactions for optimizing mechanical performance.

Biological studies conducted using *E. coli* and *S. aureus* as model microorganisms provided further insights into the impact of $Ti_3C_2T_x$ MXene on hydrogel bioactivity. While MXenes have been widely studied for its potential antibacterial properties, our findings indicate that its primary effect in this system was not antimicrobial activity, but rather ROS scavenging and enhanced bacterial viability. The antibacterial effect did not exceed 36% in any of the tested samples, with most compositions maintaining bacterial viability close to 100% over 72 h. A slight reduction in bacterial proliferation was observed when CHT was incorporated into the system, yet overall, the modified hydrogels did not exhibit strong biostatic or biocidal effects.

Further analysis of intracellular ROS levels provided a mechanistic understanding of these observations. The introduction of $Ti_3C_2T_x$ MXene led to a decrease in ROS generation, suggesting that the material acted as a free-radical scavenger. This antioxidant effect, while often beneficial in mammalian cell environments, plays a more complex role in bacterial systems, where oxidative stress is a key factor in immune defense mechanisms. Interestingly, this ROS-modulating effect

was diminished when CHT was introduced into the hydrogel matrices, indicating that the interaction between MXenes and other polymeric components may influence its biological activity.

A crucial finding of our study is the role of electrostatic interactions between the negatively charged $Ti_3C_2T_x$ MXene nanosheets and the positively charged chitosan polymer within the hydrogel network. These strong interactions likely alter the MXene surface charge distribution and partially mask reactive sites responsible for ROS scavenging. Consequently, the antioxidant capacity of MXenes is reduced in ALG/CHT composites, which correlates with the observed lower efficiency in ROS neutralization and altered antibacterial responses. This interplay highlights how tuning the surface charge through polymer selection can modulate MXene's redox behavior and biological performance, offering a valuable strategy for designing hydrogel composites with tailored ROS modulation and biocompatibility.

Overall, our study highlights the multifaceted role of $Ti_3C_2T_x$ MXene in hydrogel systems, demonstrating their ability to modify structural properties and influence biological interactions beyond traditional antibacterial paradigms. These findings suggest that MXenes-modified hydrogels could be explored in contexts where oxidative stress modulation and biocompatibility are desirable features, such as tissue engineering and advanced wound dressings. However, further studies are needed to assess their performance in mammalian systems and to tailor their functionalization toward specific therapeutic goals. Such research should focus on optimizing MXene's functional properties within hydrogel networks to strike a balance between bioactivity, mechanical stability, and potential antimicrobial performance in targeted applications. Importantly, while our results provide valuable insights into ROS modulation and hydrogel-microbe interactions, they do not replace the need for comprehensive mammalian cytocompatibility assessments. Therefore, subsequent investigations should prioritize validating these materials in relevant eukaryotic models to thoroughly assess their safety and effectiveness in clinical contexts.

Author contributions

M. J.: conceptualization, data curation, supervision, validation, methodology, formal analysis, investigation, writing – original draft, writing – review & editing, and visualization; I. N.: investigation; A. G.: investigation; D. B.: investigation; M. O.: investigation; D. M.: investigation; A. M. J.: conceptualization, methodology, formal analysis, writing – review & editing, supervision, project administration, and funding acquisition.

Conflicts of interest

There are no conflicts to declare.

Data availability

Data for this article, including results from SEM, EDS, XRD, FTIR, zeta potential measurements, DLS, dynamic particle analysis for the Ti_3AlC_2 MAX phase, and SEM, EDS, XRD, FTIR, UV-Vis spectroscopy, Tyndall effect analysis, zeta potential measurements, DLS, dynamic particle analysis, and Raman spectroscopy for the Ti_3AlC_2 MAX phase and $Ti_3C_2T_x$ MXene, as well as, data from microscopic observations, SEM, porosity analysis, Raman spectroscopy, FTIR, XRF, and oscillatory rheological measurements, for unmodified hydrogel matrices and enriched with $Ti_3C_2T_x$ MXene, and antibacterial properties studies (including agar plate culture results presented as colony forming units, optical density measurements at 610 nm, and fluorescence intensity from fluorescent probe assays), are available openly at Repository for Open Data RepOD at **https://doi.org/10.18150/GXFGEK**.

Acknowledgements

This work was funded by the National Science Centre (NCN) within the framework of the research project 'OPUS-18' (UMO-2019/35/B/ST5/02538). M. J. acknowledges funding from the National Science Centre, within the framework of the research project 'PRELUDIUM-22' (UMO-2023/49/N/ST11/03574). D.B. acknowledges funding from the National Science Centre, within the framework of the research project 'PRELUDIUM-21' (UMO-2022/45/N/ST5/02906). M. J. and D. B. further acknowledge financial support by the Foundation for Polish Science (FNP, Scholarship START programme) and from the ID-UB project (Scholarship Plus program).

References

1 E. M. Ahmed, F. S. Aggor, A. M. Awad and A. T. El-Aref, *Carbohydr. Polym.*, 2013, **91**, 693–698.
2 N. A. Peppas, B. V. Slaughter and M. A. Kanzelberger, in *Polymer Science: A Comprehensive Reference*, ed. K. Matyjaszewski and M. Möller, Elsevier, Amsterdam, 2012, DOI: **10.1016/B978-0-444-53349-4.00226-0**, pp. 385–395.
3 Z. Ahmad, S. Salman, S. A. Khan, A. Amin, Z. U. Rahman, Y. O. Al-Ghamdi, K. Akhtar, E. M. Bakhsh and S. B. Khan, *Gels*, 2022, **8**, 167.
4 S. Bashir, M. Hina, J. Iqbal, A. H. Rajpar, M. A. Mujtaba, N. A. Alghamdi, S. Wageh, K. Ramesh and S. Ramesh, *Polymers (Basel)*, 2020, **12**(11), 2702.
5 S. K. Singh, A. Dhyani and D. Juyal, *Pharma Innovation*, 2017, **6**, 25.
6 F. Ullah, M. B. H. Othman, F. Javed, Z. Ahmad and H. M. Akil, *Mater. Sci. Eng.: C*, 2015, **57**, 414–433.
7 Q. Chai, Y. Jiao and X. Yu, *Gels*, 2017, **3**(1), 6.
8 S. H. Aswathy, U. Narendrakumar and I. Manjubala, *Heliyon*, 2020, **6**, e03719.
9 J. Liu, G. Chinga-Carrasco, F. Cheng, W. Xu, S. Willför, K. Syverud and C. Xu, *Cellulose*, 2016, **23**, 3129–3143.
10 I. M. El-Sherbiny and M. H. Yacoub, *Glob. Cardiol. Sci. Pract.*, 2013, **2013**, 38.
11 J. Li and D. J. Mooney, *Nat. Rev. Mater.*, 2016, **1**, 16071.

12 H. Mengyuan, W. Changlin, X. Tong, D. Ping, Y. Xiaojun, S. Huaying, L. Congying, G. Peng and C. Zhufeng, *Polym. Bull.*, 2023, **80**, 7101–7144.
13 E. M. Ahmed, *J. Adv. Res.*, 2015, **6**, 105–121.
14 H. J. Kong, D. Kaigler, K. Kim and D. J. Mooney, *Biomacromolecules*, 2004, **5**, 1720–1727.
15 M. Ishihara, K. Obara, T. Ishizuka, M. Fujita, M. Sato, K. Masuoka, Y. Saito, H. Yura, T. Matsui, H. Hattori, M. Kikuchi and A. Kurita, *J. Biomed. Mater. Res. A*, 2003, **64**, 551–559.
16 B. Yan, J. C. Boyer, D. Habault, N. R. Branda and Y. Zhao, *J. Am. Chem. Soc.*, 2012, **134**, 16558–16561.
17 F. Fan, S. Saha and D. Hanjaya-Putra, *Front. Bioeng. Biotechnol.*, 2021, **9**, 718377.
18 N. Kandemir, W. Vollmer, N. S. Jakubovics and J. Chen, *Sci. Rep.*, 2018, **8**, 10893.
19 K. Yang, Q. Han, B. Chen, Y. Zheng, K. Zhang, Q. Li and J. Wang, *Int. J. Nanomed.*, 2018, **13**, 2217–2263.
20 M. A. Ortega, D. De Leon-Oliva, D. L. Boaru, O. Fraile-Martinez, C. García-Montero, R. Diaz, S. Coca, S. Barrena-Blázquez, J. Bujan, N. García-Honduvilla, M. A. Saez, M. Álvarez-Mon and J. V. Saz, *Gels*, 2023, **9**(8), 617.
21 M. Derakhshi, S. Daemi, P. Shahini, A. Habibzadeh, E. Mostafavi and A. A. Ashkarran, *J. Funct. Biomater.*, 2022, **13**, 27.
22 M. Jakubczak and A. M. Jastrzębska, *Front. Chem.*, 2021, **9**, 685014.
23 M. Jakubczak, A. Szuplewska, A. Rozmysłowska-Wojciechowska, A. Rosenkranz and A. M. Jastrzębska, *Adv. Funct. Mater.*, 2021, **31**, 2103048.
24 A. Szuplewska, D. Kulpińska, M. Jakubczak, A. Dybko, M. Chudy, A. Olszyna, Z. Brzózka and A. M. Jastrzębska, *Adv. Drug Delivery Rev.*, 2022, **182**, 114099.
25 M. Naguib, M. Kurtoglu, V. Presser, J. Lu, J. Niu, M. Heon, L. Hultman, Y. Gogotsi and M. W. Barsoum, *Adv. Mater.*, 2011, **23**, 4248–4253.
26 M. Naguib, M. W. Barsoum and Y. Gogotsi, *Adv. Mater.*, 2021, **33**, 2103393.
27 M. Naguib, V. N. Mochalin, M. W. Barsoum and Y. Gogotsi, *Adv. Mater.*, 2014, **26**, 992–1005.
28 Y. Ren, Q. He, T. Xu, W. Zhang, Z. Peng and B. Meng, *Biosensors*, 2023, **13**, 495.
29 Y.-Z. Zhang, J. K. El-Demellawi, Q. Jiang, G. Ge, H. Liang, K. Lee, X. Dong and H. N. Alshareef, *Chem. Soc. Rev.*, 2020, **49**, 7229–7251.
30 F. Damiri, M. H. Rahman, M. Zehravi, A. A. Awaji, M. Z. Nasrullah, H. A. Gad, M. Z. Bani-Fwaz, R. S. Varma, M. O. Germoush, H. S. Al-Malky, A. A. Sayed, S. Rojekar, M. M. Abdel-Daim and M. Berrada, *Materials*, 2022, **15**(5), 1666.
31 K. Xie, J. Wang, S. Xu, W. Hao, L. Zhao, L. Huang and Z. Wei, *Mater. Des.*, 2023, **228**, 111867.
32 A. Iqbal, J. Hong, T. Y. Ko and C. M. Koo, *Nano Convergence*, 2021, **8**, 9.
33 R. P. Pandey, P. A. Rasheed, T. Gomez, K. Rasool, J. Ponraj, K. Prenger, M. Naguib and K. A. Mahmoud, *ACS Appl. Nano Mater.*, 2020, **3**, 11372–11382.
34 K. Rasool, R. P. Pandey, P. A. Rasheed, S. Buczek, Y. Gogotsi and K. A. Mahmoud, *Mater. Today*, 2019, **30**, 80–102.
35 K. Rasool, K. A. Mahmoud, D. J. Johnson, M. Helal, G. R. Berdiyorov and Y. Gogotsi, *Sci. Rep.*, 2017, **7**, 1598.
36 K. Rasool, M. Helal, A. Ali, C. E. Ren, Y. Gogotsi and K. A. Mahmoud, *ACS Nano*, 2016, **10**, 3674–3684.
37 M. A. K. Purbayanto, M. Jakubczak, D. Bury, V. G. Nair, M. Birowska, D. Moszczyńska and A. Jastrzębska, *ACS Appl. Nano Mater.*, 2022, **5**, 5373–5386.
38 T. Wojciechowski, A. M. Jastrzębska, A. S. Vasilchenko, M. Jakubczak, M. Wolska-Pietkiewicz, A. Rozmysłowska-Wojciechowska, D. Moszczyńska, A. Olszyna and W. Ziemkowska, *Nano-Struct. Nano-Objects*, 2022, **29**, 100820.
39 M. Jakubczak, E. Karwowska, A. Rozmysłowska-Wojciechowska, M. Petrus, J. Woźniak, J. Mitrzak and A. M. Jastrzębska, *Materials*, 2021, **14**, 182.
40 A. Wojciechowska, M. Jakubczak, D. Moszczyńska, A. Wójcik, K. Prenger, M. Naguib and A. M. Jastrzębska, *Biomater. Adv.*, 2023, **153**, 213581.
41 H. J. Shields, A. Traa and J. M. Van Raamsdonk, *Front. Cell Dev. Biol.*, 2021, **9**, 628157.
42 M. Carey and M. W. Barsoum, *Mater. Today Adv.*, 2021, **9**, 100120.
43 T. Habib, X. Zhao, S. A. Shah, Y. Chen, W. Sun, H. An, J. L. Lutkenhaus, M. Radovic and M. J. Green, *npj 2D Mater. Appl.*, 2019, **3**, 8.
44 B. Anasori and Y. Gogotsi, *Graphene 2D Mater.*, 2022, **7**, 75–79.
45 M. Naguib, J. Come, B. Dyatkin, V. Presser, P.-L. Taberna, P. Simon, M. W. Barsoum and Y. Gogotsi, *Electrochem. Commun.*, 2012, **16**, 61–64.
46 M. Askkar Deen, H. Kumar Rajendran, R. Chandrasekar, D. Ghosh and S. Narayanasamy, *FlatChem*, 2024, **47**, 100734.
47 P. P. Michałowski, M. Anayee, T. S. Mathis, S. Kozdra, A. Wójcik, K. Hantanasirisakul, I. Jóźwik, A. Piątkowska, M. Możdżonek, A. Malinowska, R. Diduszko, E. Wierzbicka and Y. Gogotsi, *Nat. Nanotechnol.*, 2022, **17**, 1192–1197.
48 M. Mozafari and M. Soroush, *Mater. Adv.*, 2021, **2**, 7277–7307.
49 Q. Wu, Y. Wang, P. Li, S. Chen and F. Wu, *Appl. Phys. A*, 2021, **127**, 822.
50 D. Liu, T. Li, W. Sun, W. Zhou and G. Zhang, *ACS Omega*, 2022, **7**, 31945–31953.
51 N. U. Kiran, A. B. Deore, M. A. More, D. J. Late, C. S. Rout, P. Mane, B. Chakraborty, L. Besra and S. Chatterjee, *ACS Appl. Electron. Mater.*, 2022, **4**, 2656–2666.
52 M. Jakubczak, A. Wojciechowska, D. F. Zambrano, D. Moncada, M. Birowska, D. Moszczyńska, K. Eisawi, M. Naguib, A. Rosenkranz and A. M. Jastrzębska, *Appl. Mater. Today*, 2023, **35**, 101925.
53 M. Alhabeb, K. Maleski, B. Anasori, P. Lelyukh, L. Clark, S. Sin and Y. Gogotsi, *Chem. Mater.*, 2017, **29**, 7633–7644.
54 M. Garg and A. Thakur, *J. Mater. Sci.*, 2023, **58**, 34–45.
55 F. D. Martinez-Garcia, T. Fischer, A. Hayn, C. T. Mierke, J. K. Burgess and M. C. Harmsen, *Gels*, 2022, **8**, 535.
56 E.-R. Janeček, J. R. McKee, C. S. Y. Tan, A. Nykänen, M. Kettunen, J. Laine, O. Ikkala and O. A. Scherman, *Angew. Chem., Int. Ed.*, 2015, **54**, 5383–5388.

57 Q. Wang, Y. Zhang, Y. Ma, M. Wang and G. Pan, *Mater. Today Bio*, 2023, **20**, 100640.
58 Y. Jiang, N. Krishnan, J. Heo, R. H. Fang and L. Zhang, *J. Control Release*, 2020, **324**, 505–521.
59 T. Hu, G.-P. Wu, H. Bu, H. Zhang, W.-X. Li, K. Song and G.-B. Jiang, *Chem. Eng. J.*, 2022, **450**, 138201.
60 X. Tang, X. Wang, Y. Sun, L. Zhao, D. Li, J. Zhang, H. Sun and B. Yang, *Adv. Funct. Mater.*, 2021, **31**, 2105718.
61 C. Huang, Q. Ye, J. Dong, L. Li, M. Wang, Y. Zhang, Y. Zhang, X. Wang, P. Wang and Q. Jiang, *Smart Mater. Med.*, 2023, **4**, 1–14.
62 W. K. Jung, H. C. Koo, K. W. Kim, S. Shin, S. H. Kim and Y. H. Park, *Appl. Environ. Microbiol.*, 2008, **74**, 2171–2178.
63 E. A. Taylor and E. Donnelly, *Bone*, 2020, **139**, 115490.
64 J. W. Pinder, G. H. Major, D. R. Baer, J. Terry, J. E. Whitten, J. Čechal, J. D. Crossman, A. J. Lizarbe, S. Jafari, C. D. Easton, J. Baltrusaitis, M. A. van Spronsen and M. R. Linford, *Appl. Surf. Sci. Adv.*, 2024, **19**, 100534.
65 M. Králik and M. Kopani, *J. Electr. Eng.*, 2023, **74**, 218–227.
66 A. Sarycheva and Y. Gogotsi, *Chem. Mater.*, 2020, **32**, 3480–3488.
67 K. Shevchuk, A. Sarycheva, C. E. Shuck and Y. Gogotsi, *Chem. Mater.*, 2023, **35**, 8239–8247.
68 M. Z. I. Mollah, M. R. I. Faruque, D. A. Bradley, M. U. Khandaker and S. A. Assaf, *Radiat. Phys. Chem.*, 2023, **202**, 110500.
69 M. Shayan Asenjan, M. Asl Farshbaf, M. K. Razavi Aghjeh, A. Tavakoli and M. Rezaei, *Macromolecules*, 2024, **57**, 3993–4006.
70 G. Lawrie, I. Keen, B. Drew, A. Chandler-Temple, L. Rintoul, P. Fredericks and L. Grøndahl, *Biomacromolecules*, 2007, **8**, 2533–2541.
71 R. López-Núñez, *Appl. Sci.*, 2022, **12**, 6944.
72 M. F. Ahmed, S. Yasar and S. H. Cho, *Med. Phys.*, 2018, **45**, 5543–5554.
73 N. H. Thang, T. B. Chien and D. X. Cuong, *Gels*, 2023, **9**, 523.
74 Y. Yang, Y. Ren, W. Song, B. Yu and H. Liu, *Mater. Des.*, 2022, **223**, 111086.
75 J. Shao, C. Ruan, H. Xie, Z. Li, H. Wang, P. K. Chu and X. F. Yu, *Adv. Sci.*, 2018, **5**, 1700848.
76 C. Xing, S. Chen, X. Liang, Q. Liu, M. Qu, Q. Zou, J. Li, H. Tan, L. Liu, D. Fan and H. Zhang, *ACS Appl. Mater. Interfaces*, 2018, **10**, 27631–27643.
77 D. R. Ningrum, W. Hanif, D. F. Mardhian and L. A. T. W. Asri, *Polymers*, 2023, **15**, 468.
78 R. Athavale, N. Sapre, V. Rale, S. Tongaonkar, G. Manna, A. Kulkarni and M. M. Shirolkar, *Mater. Lett.*, 2022, **308**, 131114.
79 Z. Chen, W. Cao, Y. Liu, H. Liu, J. Ru, M. Yin, X. Luo, Y. Zhang and F. Chen, *Int. J. Biol. Macromol.*, 2024, **279**, 135527.
80 A. Jastrzebska, A. Szuplewska, A. Rozmysłowska-Wojciechowska, J. Mitrzak, T. Wojciechowski, M. Chudy, D. Moszczyńska, A. Wójcik, K. Prenger and M. Naguib, *ACS Sustainable Chem. Eng.*, 2020, **8**, 7942–7951.
81 Z. Qi, S. Wang, Y. Li, L. Wang, L. Zhao, Q. Ge and J. Z. Zhang, *Ceram. Int.*, 2021, **47**, 16555–16561.
82 H. Geng, Y. Ren, G. Qin, T. Wen, Q. Liu, H. Xu and W. He, *RSC Adv.*, 2022, **12**, 11128–11138.
83 C. Wei, P. Tang, Y. Tang, L. Liu, X. Lu, K. Yang, Q. Wang, W. Feng, Q. T. H. Shubhra, Z. Wang and H. Zhang, *Adv. Healthcare Mater.*, 2022, **11**, 2200717.
84 J. Liu, W. Lu, X. Lu, L. Zhang, H. Dong and Y. Li, *Nano Res.*, 2022, **15**, 2558–2566.
85 M. Fu, C. Yang and G. Sun, *Mol. Immunol.*, 2023, **163**, 48–62.
86 Y. E. Kim and J. Kim, *ACS Appl. Mater. Interfaces*, 2022, **14**, 23002–23021.
87 M. Mittal, M. R. Siddiqui, K. Tran, S. P. Reddy and A. B. Malik, *Antioxid Redox Signal*, 2014, **20**, 1126–1167.
88 J. Brito, H. Hlushko, A. Abbott, A. Aliakseyeu, R. Hlushko and S. A. Sukhishvili, *ACS Appl. Mater. Interfaces*, 2021, **13**, 41372–41395.
89 N. H. Nguyen, Z. Lu, A. Elbourne, K. Vasilev, I. Roohani, H. Zreiqat and V. K. Truong, *Mater. Today Bio*, 2024, **26**, 101069.
90 Y. Hui, X. Zheng, Z. Zheng, C. Wu, Y. Hao and B. Zhou, *ACS Omega*, 2024, **9**, 47964–47975.
91 A. Szerlauth, S. Varga and I. Szilagyi, *ACS Biomater. Sci. Eng.*, 2023, **9**, 5622–5631.

